JOURNAL OF MATERIALS SCIENCE 37 (2002) 629–636

# The role of starting powder size on the compressive response of stand-alone plasma-sprayed alumina coatings

R. W. TRICE*, C. BATSON‡, C. SCHARFF§, K. T. FABER
*Department of Materials Science and Engineering, Robert R. McCormick School of Engineering and Applied Science, Northwestern University, Evanston, Illinois 60208, USA*
*E-mail: k-faber@northwestern.edu*

Cylindrical stand-alone tubes of plasma-sprayed alumina were tested in uniaxial compression at room temperature, using strain gages to monitor axial strains. The effect of lamella size on the mechanical response was investigated by employing different starting powders to fabricate samples. The average powder sizes investigated included 9 $\mu$m, 19 $\mu$m and 32 $\mu$m alumina; the resulting effective lamella diameters were 10 $\mu$m, 28 $\mu$m, and 55 $\mu$m, respectively. Similar stress-strain hysteresis was observed on unloading in all tubes, independent of lamella size. A strong correlation between the failure stress and the cumulative strain at failure was also observed for tubes fabricated from the three powders. For samples with approximately constant densities, tubes plasma sprayed with the 9 $\mu$m powder exhibited greater moduli than tubes sprayed from either 19 or 32 $\mu$m powders. This difference was attributed to the greater percentage of unmelted $\alpha$-$Al_2O_3$ in the coating.


## 1. Introduction

Plasma-sprayed coatings are frequently used in thermal barrier or wear resistant applications. In these applications, stresses can be indirectly applied to the coating via stresses directly supported by the substrate (the stress applied to the coating will be dependent on its modulus). Thermal stresses can also arise upon heating and/or cooling due to coefficient of thermal expansion differences between the coating and substrate. In both cases, these stresses can cause cracking, delamination and/or spalling. As such, it is critical to know the intrinsic mechanical properties of *the coating* so that the mechanical properties of the coating/substrate system can be engineered to minimize potential problems. Also, the intrinsic properties of each constituent are often needed for failure and life prediction models.

As is well established, plasma-sprayed coatings are assembled from thin, flattened particles that result from the collision of melted powders with a substrate. How these flattened particles or lamellae stack on top of each other during each raster of the plasma gun will determine the amount and type of porosity, and other microstructural defects in the coating. These defects, in turn, will ultimately influence the mechanical properties of the coating. Previous research has focused on measuring the intrinsic response of plasma-sprayed coatings [1–6]. A study of the basic deformation mechanisms in compression loaded plasma-sprayed coatings of alumina has been addressed [6]. These results were correlated with models presented in Sammis and Ashby [7] and Ashby and Hallam [8] where they considered the effects of both porosity and microcracks on crack initiation and propagation in compressively loaded brittle materials. In plasma-sprayed materials, the porosity (primarily between lamellae) and microcracks (within lamellae) interact with the applied compressive stress. Cracks nucleate and/or propagate from these existing defects, as the models [7, 8] would predict, along lamella boundaries. Nucleation and/or propagation of these defects causes the familiar hysteretic behavior often observed on unloading of plasma-sprayed materials. The numerous crack sites link up, resulting in long cracks oriented parallel with the loading direction. Thus, narrow columns are formed. These columns are inherently unstable in compression, and the sample fails due to localized buckling.

In the current research, we have varied the size of the lamellae by starting with different powder sizes of alumina. Stand-alone coatings sprayed with three different sized powders were then tested in compression using a cylindrical geometry and the results were analyzed.

*Present Address*: Purdue University, School of Materials Engineering, West Lafayette, IN 47907.
‡*Present Address*: University of California, Santa Barbara, Department of Materials, Santa Barbara, CA 93106.
§*Present Address*: Cornell Law School, Ithaca, NY 14853.

TABLE I Overview of powders and spray parameters

| Sample designation | Injector type | Power, kW | Spray distance, cm | Radial distance, mm | Primary gas flow[d], slm | Carrier gas flow[e], slm |
|---|---|---|---|---|---|---|
| D9[a] | SPPS | 35 | 7 | 10 | 35 | 5 |
| D19[b] | SPPS | 35 | 7 | 10 | 35 | 5 |
| D32[c] | Conventional | 40 | 7 | 9 | 35 | 5 |

[a]Praxair Specialty Ceramics, 9.1 $\mu$m diameter, Powder 1110 HP, Woodinville, WA.
[b]Sumitomo Chemical America, 19.0 $\mu$m diameter, Powder AA-18, New York, NY.
[c]Norton Company, 32.5 $\mu$m diameter, Powder 153 TSP 9349, Worcester, MA.
[d]The primary gas was argon.
[e]The carrier gas was argon.
(The following spray parameters were held constant: $H_2$ secondary gas flow of 11 slm, cooling air of 30 psi, gun translation of 350 mm/s.)

Compression loading was chosen because it represents actual loading conditions experienced by both TBC and wear resistant coatings during normal service. It should be noted that while alumina is not a feasible TBC, the testing methods described could easily be adapted for stand-alone coatings of the standard TBC material (7 wt% $Y_2O_3$–$ZrO_2$).

## 2. Experimental procedure

### 2.1. Sample fabrication and physical testing

The plasma-spray equipment used to fabricate specimens included an A-3000S Plasma Technik control system with an F4 gun. The gun assembly was mounted on a seven-axis ASEA Brown and Boveri IRB 2000 robot. The powder was fed into either a small-particle plasma-spray (SPPS) injector [9] or an externally-mounted straight-thru injector, depending on the powder size, using a twin-10 disc feeder (Plasma-Technik). Three different powders were investigated, with the particulars of each alumina powder revealed in Table I and SEM micrographs of each powder shown in Fig. 1. Average powder diameters of 9.1, 19.0, and 32.5 $\mu$m were sprayed. Samples made from these powders were designated D9, D19, and D32, respectively.

The details of fabricating stand-alone cylindrical plasma-sprayed coatings have been published previously [6] and will only be reviewed here. Stand-alone coating specimens were manufactured by first plasma-spraying aluminum on a rotating 300 mm long by 13 mm diameter alumina rod. Following a light surface abrade and ethanol cleaning, a 200–400 $\mu$m thick alumina layer was sprayed on the aluminum-coated alumina rod using the spray parameters listed in Table I. The spray parameters were equivalent for the D9 and D19 powders, with increased power required to melt the larger D32 powders. Spray distance was measured from the center hole of the injector to the substrate and radial distance was defined as the distance from the injector to the centerline of the plume. Cooling air at a pressure of 0.33 MPa was forced down the open hole of the rotating tube during the spraying of the alumina coatings. Because the spray parameters generally cannot be the same for vastly different size powders, where possible, comparisons were made based on density.

Samples were cut from the long rod into approximately ten 25.4 mm long tubes, with the faces of each tube machined parallel. The tubes were immersed in a weak solution of HCl to dissolve the aluminum, releasing the plasma-sprayed alumina tube from the underlying alumina substrate. The stand-alone tubes were then dried and their physical properties measured. The bulk density of the stand-alone tubes made from each powder was determined by the immersion method [10], with density variations observed in samples cut from the same rod. Using $K_\alpha$ x–ray diffraction and calibration standards described in previous research [11], the volume percentage of $\alpha$-$Al_2O_3$ was measured for select samples, with the remaining coating comprised of $\gamma$-$Al_2O_3$. Based on the amount of each phase, a theoretical density was calculated for each coating assuming densities of 3.65 and 4.0 g/cm$^3$ for $\gamma$-$Al_2O_3$ and $\alpha$-$Al_2O_3$, respectively.

A single scan of the plasma-gun over a cylindrical alumina substrate was used to isolate individual lamellae for characterization. The processing parameters for single lamella production were identical to those described in Table I, with the following exceptions. The scanning speed was 1 m/s and the powder disc feed rate was slowed from 3 to 0.1 (relative units). These processing changes were expected to result in single lamellae representative of those found in coatings.

The equivalent diameter ($d_{\text{equivalent}}$) and degree of splashing ($\Phi$) of at least eight individual lamellae from each powder were characterized using the following equations [12]:

$$d_{\text{equivalent}} = \left(\frac{4A}{\pi}\right)^{\frac{1}{2}}$$

$$\Phi = \left(\frac{1}{4\pi}\right)\left(\frac{P^2}{A}\right)$$

where $A$ is the area and $P$ is the perimeter of the lamella. Both $A$ and $P$ were determined using image processing software (NIH Image Software) on digitally captured SEM images. Debris of alumina that had splashed from the original lamella were not included in either $A$ or $P$. Values of $\Phi = 1$ indicate no splashing, whereas $\Phi > 1$ is an indication that splashing was observed.

Scanning electron microscopy (SEM) images were taken of polished cross-sections of each coating. Cross-sections of D9 were polished then etched for 5 minutes in concentrated $H_2SO_4$ at 210°C. The acid etch revealed the microstructure of the coatings in greater detail.

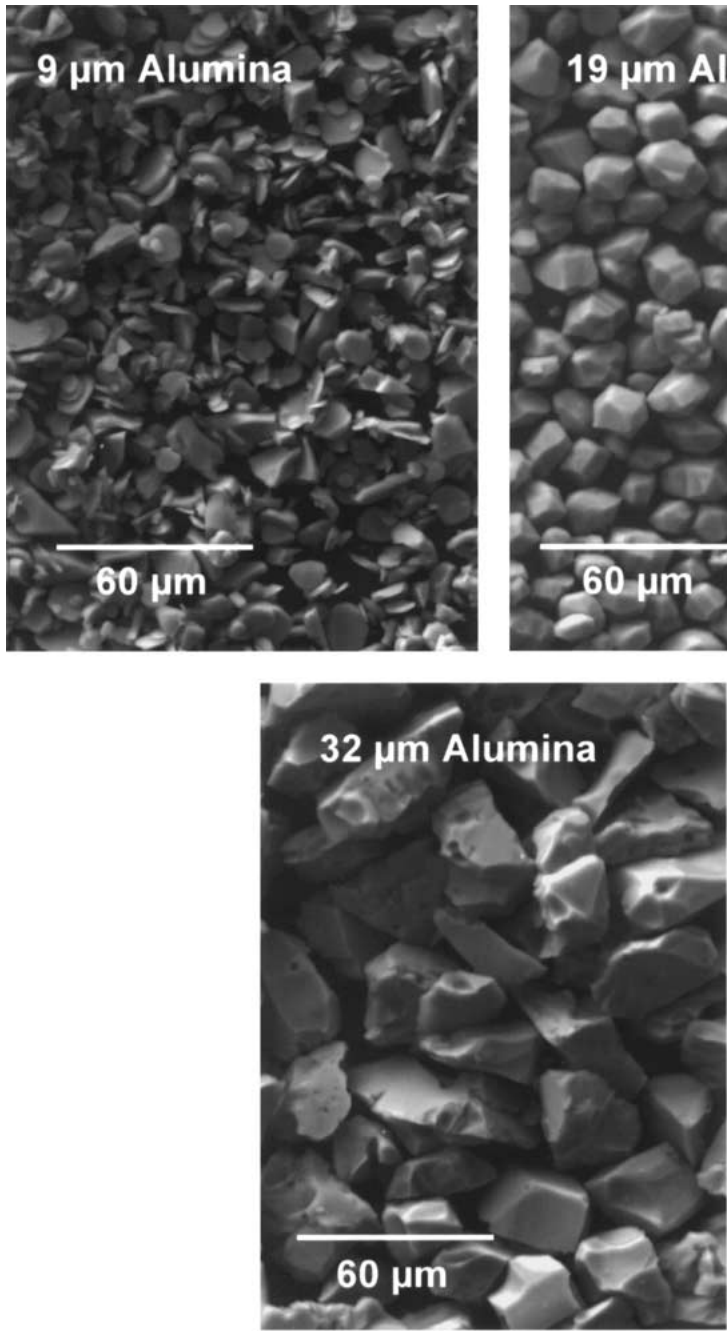


*Figure 1* SEM micrographs of the three powders studied.

## 2.2. Mechanical testing

A schematic of a stand-alone coating is shown in Fig. 2, showing the orientation of the strain gages used to monitor the strain response. Gages were bonded with a small amount of epoxy[¶], with a bondline thickness of 5–10 $\mu$m as measured in the SEM. Two axially oriented gages, bonded on opposites sides of each tube, were used to measure the axial strain response ($\varepsilon_{22}$). The difference in axial strain response between the two gages was used to assess alignment and was typically less than 6%.

Samples were compression loaded between two steel platens in a commercial load frame*, such that the long axis of the lamellae were oriented parallel with the loading direction. Tungsten carbide (WC) inserts were

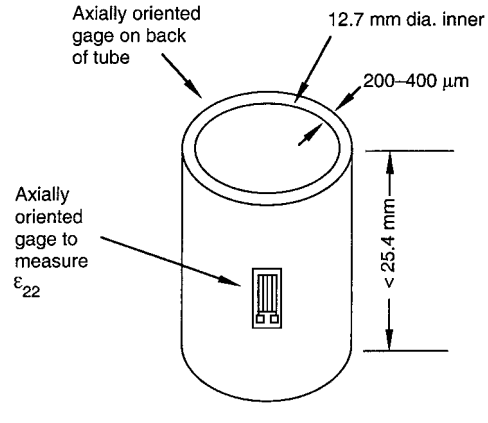


*Figure 2* A schematic of stand-alone coating test sample. Samples were axially loaded in compression.

[¶] Measurements Group, AE-10/15 Adhesive Kit, Raleigh, N.C.

* MTS, 808 Electromechanical Test System, Minneapolis, MN.

placed between the platens and the sample to prevent damage of the soft steel by the ceramic tube. Also, self-adjusting spherical washers were used to assist load alignment. The loading profile, under load control, was cyclic loading with monotonically increasing applied stresses. The maximum applied stress was increased with each successive loading/unloading cycle. Beginning at 25 MPa, loads were increased to achieve a 25 MPa increase in the applied stress with each cycle. For example, sequential loading/unloading profiles to 25 MPa, 50 MPa, 75 MPa . . . and 200 MPa maximum load were performed. Beyond 200 MPa, the stress increment was 50 MPa through failure. Strain was monitored during loading and unloading. The loading and unloading rate was 20 N/s.

The stress in each tube was calculated by dividing load by cross-sectional area. Elastic modulus in the axial direction was calculated by dividing stress by the average of the two axial gage responses in the initial linear portion of the stress-strain curve. The strain offset, or permanent deformation, of the coating was calculated by subtracting the average axial strain on loading (at 5 MPa) from the average axial strain upon unloading (also at 5 MPa). The summation of the permanent deformation for each loading/unloading cycle with the deformation just prior to failure gave the cumulative strain to fracture. Data from the two strain gages, as well as load and time, were collected at a rate of 10 $sec^{-1}$.

## 3. Results and discussion

### 3.1. Microstructural analysis

Fig. 3 shows polished cross-sections of each coating taken with a SEM. Large porosity (>1$\mu$m) was observed in polished cross-sections of the coatings, typical of most air plasma-sprayed coatings. No through-thickness cracks were observed. It is also understood that smaller porosity (<0.1$\mu$m) exists between the lamellae, resulting in ≈20% contact between adjacent lamellae [13].

Table II presents the equivalent diameter ($d_{equivalent}$) and degree of splashing ($\Phi$) for individual lamellae from each of the three powders investigated. Some radial splashing was typically observed in all lamellae, with an example from the 32 $\mu$m powder shown in Fig. 4. The conditions for splashing to occur are a complex function of the temperature and velocity of the particle and the roughness of the substrate. The equivalent diameter of the lamellae ranged from 9.6 for the 9 $\mu$m powder to 55 $\mu$m for the 32 $\mu$m powder. The fact that the $d_{equivalent}$ was approximately equal to the starting 9 $\mu$m powder size matched with experimental observations that part of the melted 9 $\mu$m diameter particle splashed away from the primary lamella. The degree of splashing was quite large, ranging from 4 for the 9 $\mu$m powder to 13 for the 19 $\mu$m and 32 $\mu$m powders. It is worth noting that $\Phi$ for the 9 $\mu$m powder is likely smaller because part of the material detached from the lamellae during splashing and was not accounted for in the analysis.

Measurements of the average lamella thickness were made from polished SEM micrographs. These varied from 1.4 $\mu$m, 1.9 $\mu$m, and 2.2 $\mu$m for the 9 $\mu$m, 18 $\mu$m, and 32 $\mu$m powders, respectively, as shown in Table II. By dividing the coating thickness by the measured lamella thickness the number of interfaces can be calculated for coatings made from each powder. This ranges from ≈200 interfaces for the D9 and D32 coatings. The number of interfaces in the D19 coating varied from ≈100 to ≈150, depending on the thickness of the samples. The number of interfaces is important as most of the submicron porosity critical for crack initiation and/or propagation in compressive loaded tubes is located between lamellae.

### 3.2. Overview of compressive test results

Table III is an overview of all the physical and mechanical results for each of the cylinders tested. The tabulated results for the 9$\mu$m powder have been

TABLE II Results of the Lamella analysis

| Powder designation | Equivalent diameter, $d_{equivalent}$, $\mu$m | Degree of splashing, ($\Phi$) | Measured Lamella thickness, $\mu$m |
|---|---|---|---|
| D9 | 9.6 ± 1.8 | 4 ± 1 | 1.4 ± 0.5 |
| D19 | 28.4 ± 5.8 | 13 ± 4 | 1.9 ± 0.5 |
| D32 | 55.0 ± 7.4 | 13 ± 4 | 2.2 ± 0.6 |

TABLE III Overview of physical and mechanical tests

| Sample designation | Thickness ($\mu$m) | $\alpha$-$Al_2O_3$ (vol%) | Density ($g/cm^3$) | Percent dense | Failure stress (MPa) | Failure strain (%) | Maximum strain (%) | Initial modulus (GPa) | Final[b] modulus (GPa) |
|---|---|---|---|---|---|---|---|---|---|
| D9d[a] | 308 | 6.1 | 3.26 | 89 | 493 | 0.70 | 0.7 | 96 | 80 |
| D9e | 307 | 7.6 | 3.16 | 86 | 295 | 0.44 | 0.53 (350 MPa) | 81 | 74 |
| D9g | 320 | 6.8 | 3.16 | 86 | 500 | 0.83 | 0.83 | 72 | 55 |
| D9h | 290 | + | 3.16 | 86 | 380 | 0.63 | 0.63 | 74 | 59 |
| D19a | 203 | 3.3 | 3.24 | 88 | 235 | 0.38 | 0.38 | 80 | 72 |
| D19d | 207 | 3.5 | 3.22 | 88 | 374 | 0.67 | 0.76 (450 MPa) | 72 | 59 |
| D19h | 297 | + | 3.27 | 89 | 432 | 0.68 | 0.68 | + | + |
| D32a | 408 | 2.8 | 3.37 | 92 | 338 | 0.50 | 0.50 | 72 | 62 |
| D32d | 405 | 3.3 | 3.36 | 92 | 517 | 0.75 | 0.74 (550 MPa) | 75 | 65 |
| D32e | 410 | + | 3.37 | 92 | 384 | 0.49 | 0.49 | 69 | + |

+Data not available

[a] 9 $\mu$m data is from reference 6.

[b] Calculated from the initial slope of the stress-strain loading response during which failure occurred.

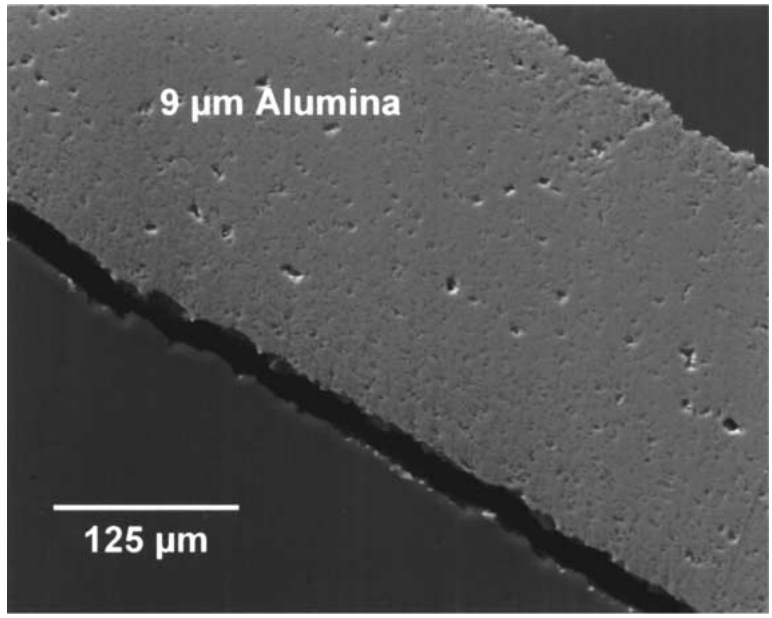


(a)

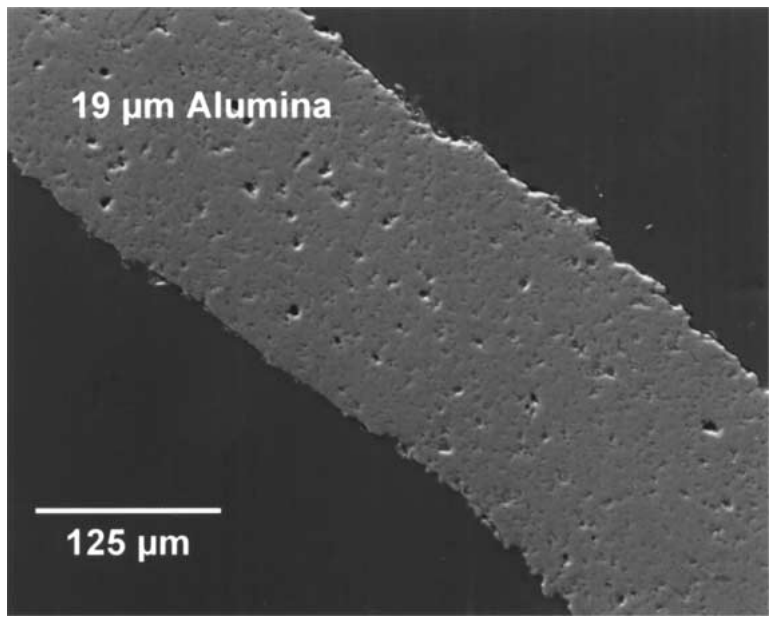


(b)

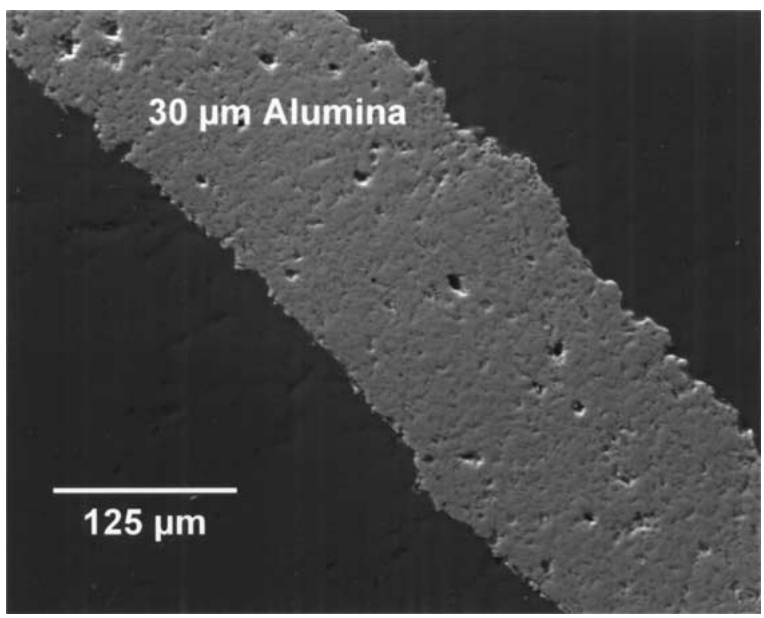


(c)

*Figure 3* SEM of polished cross-sections of the coatings studied.

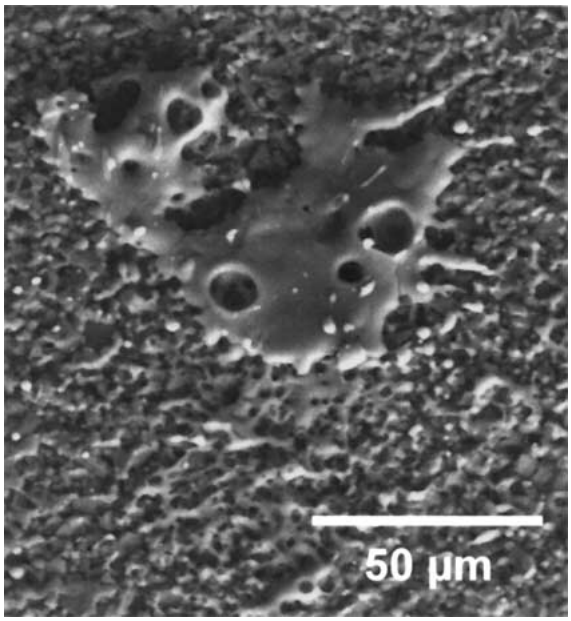


*Figure 4* Individual lamella of alumina formed from the 32 $\mu$m powder.

presented previously [6]. All of the tubes were subject to increased-stress cyclic loading. The tubes varied from 86 to 92% dense and the strength varied from 225 to 500 MPa. In some instances, tubes failed at lower loads than they had previously sustained. For example, D19d was previously loaded to 450 MPa; upon reloading the sample fractured at 374 MPa. The cumulative strain at failure for all samples ranged from 0.38 to 0.83%. Low strains were correlated with low strength. Modulus was calculated in the initial linear stress-strain region during the first loading sequence (to 25 MPa) and on final loading, just prior to fracture. In every case the as-sprayed tubes displayed a lower modulus in the final cycle than in the initial cycle. It should be noted that the strain gages used in this study, with an area of 5.25 mm$^2$, would cover $\approx$60,000 lamellae made from the 9 $\mu$m powder. The coverage varies between $\approx$8000 and $\approx$2200 lamellae for the 19 $\mu$m and 32 $\mu$m powders, respectively. Thus, an average strain is measured using these gages.

## 3.3. Mechanical response

There were two common mechanical responses observed regardless of starting powder size. These included stress-strain hysteresis and reduction in elastic modulus on repeated loading to incrementally higher stresses. Differences in the magnitude of modulus were observed, however, for the samples made from different sized powders.

### *3.3.1. Lamella size effects on stress-strain behavior*

Fig. 5 is the comparison of the mechanical response of tubes fabricated from the 3 different size powders subjected to increased cyclical loading through 200 MPa. The stress-strain responses have been offset for clarity. Significant hysteresis between the loading and unloading portions of the curve were observed for all tubes, invariant of powder size. Hysteretic behavior has been observed previously in plasma-sprayed materials [1, 4].

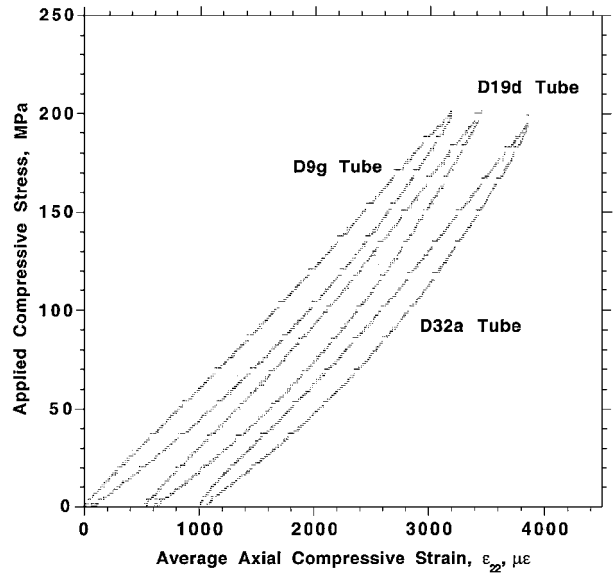


*Figure 5* Loading/unloading curves for tubes fabricated from three different powder sizes. They have been offset for clarity.

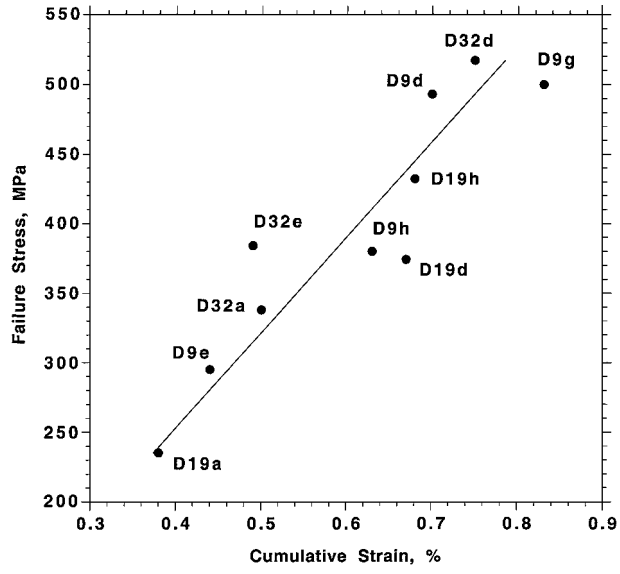


*Figure 6* Plot of failure stress versus cumulative strain for all tested samples.

The width of the hysteresis curves was approximately equal for all powders. Upon unloading, the strain did not return to zero, but rather indicated a permanent deformation for all three types of tubes. Physically, this indicates that the samples were compressed during testing. A plot of the permanent offset (not shown) was proportional to the applied stress during cyclical loading. Thus, the amount of damage with each loading/unloading cycle was also equivalent for tubes made from the same powder.

Fig. 6 reveals a strong correlation between failure stress and cumulative strain for all samples tested, independent of starting powder size. The cumulative strain, which includes the permanent deformation accumulated during each loading and unloading cycle and the deformation prior to failure, represents the total amount of damage that the sample can sustain before failure. We know from prior work [6] that the damage is typically manifested in the microstructure as microcracks which originate from pores. As such, we might expect a

correlation between the porosity (which serve as crack initiation sites) and the failure stress. A plot of failure stress versus total porosity, not shown here, for the current data revealed no correlation. This may be an indication that in compression loading the location and distribution of the porosity is more important that the total amount.

Adams and Sines have presented a general theory of the compressive strength of brittle materials [14]. They assert that in compression catastrophic failure occurs only where there is sufficient interaction between flaws and the applied stress, which is different than tension, where one flaw can result in failure. Thus, the compressive strength is dependent on total flaw distribution and not necessarily on the size of the worst flaw(s). Therefore, the primary feature size of the microstructure (i.e. lamella diameter) may be less important, as experimentally observed, than the distribution and amount of porosity that exists between adjacent lamellae. The distribution and amount of the interlamellar porosity is likely only weakly dependent on lamella size [15], but this has not been investigated for alumina. Furthermore, the expected inverse relationship between strength and porosity might be convoluted because it is difficult to distinguish between the larger porosity (small in number, but large in volume) and the smaller porosity (large in number, but small in volume). It is expected that the smaller porosity will contribute more to the crack density because many more sites are available for crack nucleation.

### 3.3.2. Modulus trends with cyclic loading

Fig. 7 compares the compressive modulus of several tubes as a function of the maximum applied stress. A decrease in modulus was noted as the cyclic load increased for all tubes tested. This trend was observed in all tubes, regardless of starting powder size. The modulus decreases steadily because the extent of damage, in the form of cracks propagating between lamellae, increases with each cycle. The effect of an increase in crack density of compressively loaded samples has previously been shown to decrease the modulus [7].

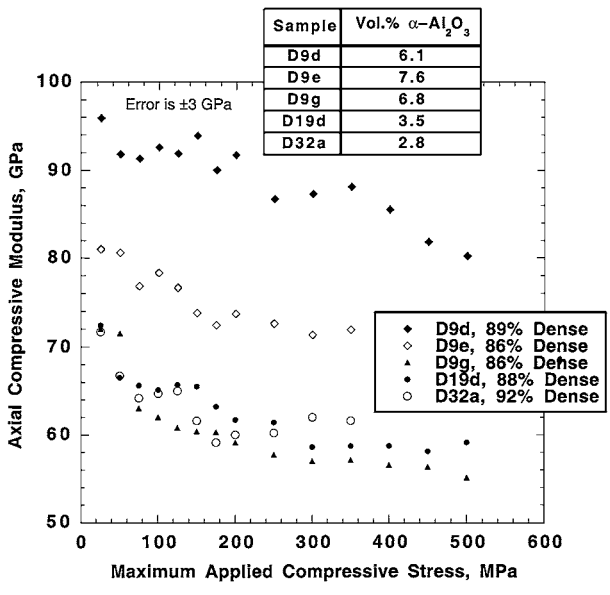


*Figure 7* Plot of compressive modulus in the axial direction as a function of the maximum applied compressive stress for several tubes.

Prior work [4] in plasma-sprayed YSZ has indicated a strong influence of porosity on compressive modulus, with a 4% increase in density doubling the modulus of samples made from the same size starting powder. This trend was observed in samples made with the 9 $\mu$m starting powder, but the effects of density were not as great. Comparison of the modulus of D9d and D9g demonstrate an ≈40% difference in modulus with a 3% difference in density. Porosity effects on samples made with 19 $\mu$m and 32 $\mu$m powders could not be made because they had similar densities, however, similar trends to those observed in samples made with the 9 $\mu$m powder would be expected.

A comparison of modulus values for samples made from the three different powders reveal some differences. For example, while D19d has a greater density (88% dense), its modulus falls within the experimental error of tube D9g, a tube with a lower density (86% dense). D32a exhibited the greatest density (92% dense) but demonstrated a modulus similar to D9g. If we were to make a D32 sample that was 88% dense, we might expect that its modulus profile as a function of applied stress would be much lower. Ultimately, the trend is that samples assembled from smaller lamellae seem to demonstrate larger compressive moduli. However, these apparent differences are not due to lamella size, but rather, correlate to the amount of unmelted particles in the coating.

One aspect of the plasma-sprayed microstructure that has been explored less vigorously is the effect of the unmelted or partially melted powders on the mechanical response of the as-sprayed coating. For alumina powders that begin as $\alpha$-$Al_2O_3$, the amount of unmelted or partially melted powders is equal to the amount of $\alpha$-$Al_2O_3$ phase in the coating [16]. An example of unmelted powders incorporated into a coating is shown in Fig. 8a. These typically appear circular in shape as compared to the flattened lamellae.

One approach to modeling the modulus of the resulting two-phase microstructure is using a rule of mixtures, where one phase is the $\gamma$-$Al_2O_3$ and the other phase is un-melted or partially melted $\alpha$-$Al_2O_3$ powders. This is shown schematically in Fig. 8b. As such, the upper value of the elastic modulus of the coating, $E_{\text{coating}}$, can be represented by the following equation:

$$E_{\text{coating}} = E^{\text{o}}_{\gamma} \exp^{-bP} V_{\gamma} + E^{\text{o}}_{\alpha} V_{\alpha}$$

where $E^{\text{o}}$ represents the pore-free elastic modulus and $V$ is the volume fraction of either the $\gamma$-$Al_2O_3$ or $\alpha$-$Al_2O_3$ phase, $P$ is the volume fraction of porosity, and $b$ is an empirical constant that is a function of the shape of the porosity [17, 18].

Based on the microstructure of plasma-sprayed coatings we can comment further on the modulus of both phases. First, unmelted particles are essentially defect free, and thus possess the modulus of 100% dense $\alpha$-$Al_2O_3$. This is approximately 400 GPa [19]. The authors were not able to find a suitable value for the intrinsic modulus of $\gamma$-$Al_2O_3$, as it is difficult to

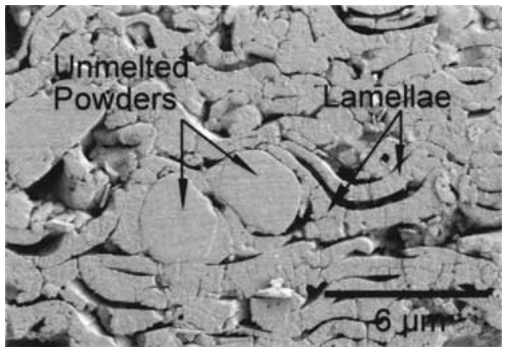


(a)

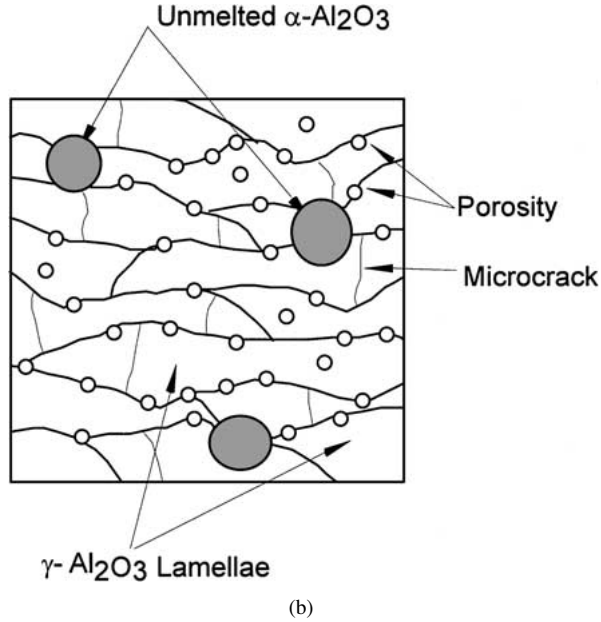


(b)

*Figure 8* (a) Polished and etched cross-section of a coating made from 9 $\mu$m powders revealing two unmelted particles. (b) Cross-sectional schematic of a plasma-sprayed coating. Shown are unmelted particles ($\alpha$-$Al_2O_3$), lamellae ($\gamma$-$Al_2O_3$) and other microstructural features including porosity and microcracks.

form due to the preference of alumina to manifest as $\alpha$-$Al_2O_3$. Estimates from the current and previous work [20] place the defect free modulus of $\gamma$-$Al_2O_3$between 70–180 GPa. However, clearly the porosity is located predominantly in the $\gamma$-$Al_2O_3$ (both inter-lamella and intra-lamella porosity)[21] and its effects on modulus must be accounted for depending on the amount, shape, and distribution of the porosity [17, 18, 22]. While the uncertainty of $E_\gamma^o$ makes it difficult to precisely model the behavior, it is clear that the unmelted powders can significantly increase the modulus of the system. For example, 3 vol% $\alpha$-$Al_2O_3$ could increase the modulus by 10–12 GPa.

The stiffening effect of the unmelted powders is observed in Fig. 7 and is believed to be responsible for the differences in the elastic modulus of coatings made from different sizes that are not attributable to density. For example, compare D9e, with an equivalent density to D9g, but a higher modulus and correspondingly more $\alpha$-$Al_2O_3$. Next, consider D9d and D19d, with slightly different densities but very different moduli. As shown in the table inset in Fig. 7, D9d has more of the stiffening $\alpha$-$Al_2O_3$phase than D19d, resulting in a greater modulus. D32a, despite being 92% dense, has only 2.8 vol% $\alpha$-$Al_2O_3$ and thus has a small modulus. Ultimately, knowing the defect-free modulus of $\gamma$-$Al_2O_3$ would greatly assist in modeling of these two phase materials.

## 4. Conclusions

The role of lamella size was found to have minimum effect on the compressive fracture properties of standalone plasma-sprayed alumina coatings. No difference in stress-strain response was noted for coatings made from 9 $\mu$m, 19 $\mu$m and 32 $\mu$m size powders that were attributable to lamella size. This result is likely specific to compression loading, as the nucleation and propagation of cracks in plasma-sprayed materials is likely controlled by the submicron porosity that exists between lamellae and is independent of the lamella size. The modulus of the coatings was found to be a function of both the amount of unmelted particles, existing as $\alpha$-$Al_2O_3$, and the porosity. Increasing the amounts of $\alpha$-$Al_2O_3$ and/or decreasing amounts of porosity were found to increase the elastic modulus. Under the spray conditions used, the $\alpha$-$Al_2O_3$ content in the coating increased with smaller starting size powder.

## References

1. E. F. REJDA, D.F. SOCIE and B. BEARDSLEY, *Fatigue Fract. Engng. Mater. Struct.* **20**(7) (1997) 1043.
2. K. F. WESLING, D. F. SOCIE and B. BEARDSLEY, *J. Amer. Ceram. Soc.* **77**(7) (1994) 1863.
3. S. R. CHOI, D. ZHU and R. A. MILLER, *Ceram. Eng. Sci. Proc.* **19**(4) (1998) 293.
4. T. A. CRUSE, B. P. JOHNSEN and A. NAGY, *J. Thermal Spray Tech.* **6**(1) (1997) 57.
5. B. P. JOHNSEN, T. A. CRUSE, R. A. MILLER and W. J. BRINDLEY, *Eng. Mater. Tech.* **117**(7) (1995) 305.
6. R. W. TRICE, D. W. PRINE and K. T. FABER, *J. Amer. Ceram. Soc.* **83**(12) (2000) 3057.
7. C. G. SAMMIS and M. F. ASHBY, *Acta Metall.* **34**(3) (1986) 511.
8. M. F. ASHBY and S. D. HALLAM, *ibid.* **34**(3) (1986) 497.
9. T. F. BERNECKI and D. R. MARRON, U.S. Patent no. 5,744,777, 1998, and U.S. Patent no. 5,858,470, 1999.
10. ASTM Standard C 373-72 (1982).
11. R. W. TRICE and K. T. FABER, *J. Amer. Ceram. Soc.* **83**(4) (2000) 889.
12. G. MONTAVON, S. SAMPATH, C. C. BERNDT, H. HERMAN and C. CODDET, in Proceedings of the International Thermal Spray Conference, May 1995, Kobe, Japan (1995) p. 365.
13. R. MCPHERSON, *Surface and Coatings Technology* **39/40** (1989) 173.
14. M. ADAMS and G. SINES, *J. Amer. Ceram. Soc.* **61**(3/4) (1978) 126.
15. ANDREW ALLEN, National Institute of Standards and Technology, private communication.
16. R. MCPHERSON, *J. Mat. Sci. Eng.* **15**(1980) 3141.
17. R. M. SPRIGGS, *J. Amer. Ceram. Soc.* **44**(12) (1961) 628.
18. R. C. ROSSI, *ibid.* **51**(8) (1968) 433.
19. D. J. GREEN, C. NADER and R. BRENZY, in "Ceramic Transactions," edited by C. A. Handwerker, J. E. Blendell and W. Kaysser (The American Ceramic Society, Westerville, OH, 1990) vol. 7, p. 345.
20. S.-H. LEIGH, C.-K. LIN and C. C. BERNDT, *J. Amer. Ceram. Soc.* **80**(8) (1997) 2093.
21. A. R. DE ARELLANO-LÓPEZ and K. T. FABER, *ibid.* **82**(8) (1999) 2204.
22. I. SEVOSTIANOV and M. KACHANOV, *Mat. Sci. Eng.-A-Struct.* **297**(1–2) (2001) 235.

*Received 24 July 2000*
*and accepted 3 August 2001*